PHYSICAL REVIEW B **73**, 235104 (2006)

Electronic structure of the α and δ phases of Bi_2O_3: A combined *ab initio* and x-ray spectroscopy study

Aron Walsh and Graeme W. Watson*
School of Chemistry, University Of Dublin, Trinity College, Dublin 2, Ireland

David J. Payne and Russell G. Edgell
Department of Chemistry, Inorganic Chemistry Laboratory, South Parks Road, Oxford OX1 3QR, United Kingdom

Jinghua Guo
Advanced Light Source, Lawrence Berkeley National Laboratory, Berkeley, California 94720, USA

Per-Anders Glans, Timothy Learmonth, and Kevin E. Smith
Department of Physics, Boston University, 590 Commonwealth Avenue, Boston, Massachusetts 02215, USA

(Received 6 April 2006; published 7 June 2006)

α-Bi_2O_3 is the thermodynamically stable phase of Bi_2O_3 at room temperature. We have performed a theoretical and experimental investigation of its electronic structure using a combination of gradient corrected density functional theory (DFT), along with x-ray photoemission and O-*K* shell x-ray absorption and emission spectroscopies. We examine the nature of bonding in α-Bi_2O_3 and in particular explore the nature of the stereochemically active Bi electron lone pair. The Bi 6*s* states are found to be concentrated at the bottom of the valence band but the states contributing to the lone pair on Bi are derived from the top of the valence band. Mixing between O 2*p* and Bi 6*s* states is found to be crucial in producing the asymmetric density on Bi. The role of the lone pair in the fast ion conductor δ-Bi_2O_3 is also investigated, through calculation of the electronic structure with $\langle 100\rangle$, $\langle 110\rangle$, and $\langle 111\rangle$ alignment of oxygen vacancies. Alignment of the vacancies along $\langle 100\rangle$ results in the most energetically favorable configuration of the δ phase, contrary to previous force field calculations and electrostatic arguments which favor the $\langle 111\rangle$ alignment.

DOI: 10.1103/PhysRevB.73.235104 PACS number(s): 71.20.−b, 79.60.−i, 71.15.Mb

I. INTRODUCTION

Bismuth sesquioxide is a pleomorphic material with at least four known polymorphs, a feature quite atypical of R_2O_3 materials.[1] These include the thermodynamically stable α phase and the metastable β and γ phases which result from the cooling of the high temperature δ phase, which is itself stable above 1000 K. Monoclinic α-Bi_2O_3 belongs to the space group $P2_1C$ and has a highly irregular structure[2,3] containing five coordinate Bi atoms with the five oxygens present on one side of the atom as shown in Fig. 1(a). Bi_2O_3 has been the subject of great interest due to its ionic conduction properties,[4,5] and its wide range of potential applications in solid oxide fuel cells[6] gas sensors,[7] and optical coatings.[8]

δ-Bi_2O_3 is a fast oxygen ion conductor and numerous experimental[9–13] and theoretical[14–17] studies have been performed on this material. The cubic δ phase with space group $Fm3m$ is a based on a defective fluorite-type lattice shown in Fig. 1(b), in which only six of the eight anion sites are occupied. This is in many ways similar to the cubic bixbyite structure[18] adopted by Tl_2O_3 where incomplete cubic close-packing of oxygen ions is based on a supercell of the fluorite structure. In δ-Bi_2O_3 each unit cell has (on average) two vacant oxygen sites which contribute to the high mobility of oxygen atoms observed experimentally. There are three possible simple configurations of the vacancies in a single unit cell, aligned along the $\langle 100\rangle$, $\langle 110\rangle$ or $\langle 111\rangle$ directions. These give rise to the three types of Bi coordination shown in Fig. 2. Conflicting previous studies have suggested each of the three different possible alignments of the oxygen vacancies along $\langle 100\rangle$,[17] $\langle 110\rangle$,[6] and $\langle 111\rangle$ (Refs. 7, 13, 14, and 19) directions. Alternatively a number of supercell configurations[20] and a statistically averaged occupation of all eight positions[21] have been considered.

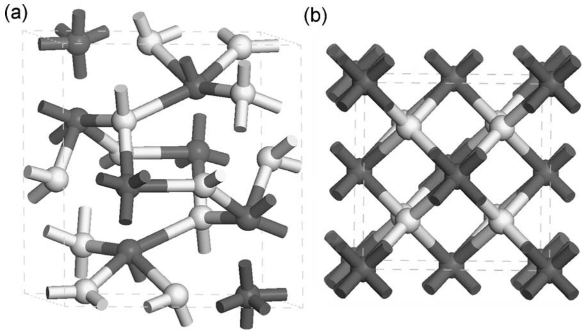

FIG. 1. The crystal structures of (a) α-Bi_2O_3 and (b) CaF_2 (fluorite). The cations are colored dark with the anion light.

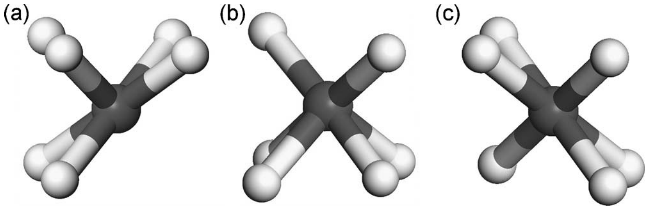

FIG. 2. Schematic representation of a single Bi ion in δ-Bi_2O_3 with oxygen vacancies aligned along the (a) $\langle 100\rangle$, (b) $\langle 110\rangle$, and (c) $\langle 111\rangle$ axes.

One issue not addressed in previous studies is the detailed electronic structure and in particular the influence of the stereochemical lone pair. The Bi(III) oxidation state results in a filled 6*s* subshell and an electronic configuration of $5d^{10}6s^{2}6p^{0}$. Classically the $6s^2$ electrons are understood to occupy an inert orbital resulting from the hybridization of Bi 6*s* and 6*p* states, which is projected out one side of the Bi atom and distorts the crystal structure. The stereochemically active Bi(III) lone pairs have also been associated with the enhanced conductivity of the δ phase.[14,22] Mairesse[23] suggested that the presence of the lone pair leads to high polarizibility of the cation network, which in turn leads to oxide ion mobility. Calculations on the oxides of Pb(II) (Refs. 24 and 25) and Sn(II) (Refs. 26 and 27) have suggested that the origin of asymmetry in ns^2 materials is not as simple as a classical lone pair theory would suggest and that the anion is required to bridge the gap between the cation *s* and *p* states by mutual mixing with both. Theoretical and experiment studies on neighboring heavy metal oxides indicate that similar mixing of between metal empty 6*s* and filled 5*d* states mediated by anion 2*p* states occurs in HgO and Tl_2O_3.[28,29] Such interaction would have clear implications for oxygen vacancy alignment and mobility in δ-Bi_2O_3.

The aim of this work is to perform a rigorous analysis of the electronic structure of α-Bi_2O_3 using a combination of theory and experiment, with particular emphasis on the formation of the Bi lone pair. The effects of the lone pair in δ-Bi_2O_3 with oxygen vacancies aligned along $\langle 100\rangle$, $\langle 110\rangle$, and $\langle 111\rangle$ will then be investigated. While δ-Bi_2O_3 is a high temperature phase and it is unlikely that the $\langle 100\rangle$, $\langle 110\rangle$ or $\langle 111\rangle$ arrangements uniquely represent the crystal structure of δ-Bi_2O_3, an examination of these idealized configurations can be used to gain insight into their formation energies and relative stabilities. A comprehensive examination of the electron density of states, electron density maps and band structure will allow for a better understanding of the nature of Bi(III) cations in Bi_2O_3.

II. METHODS

A. Computation

The electronic structures of α and δ-Bi_2O_3 were calculated using DFT as embodied in the Vienna *Ab initio* Simulation Package.[30–32] The Kohn-Sham equations[33] were solved self-consistently using an iterative matrix digitalization technique. The forces on the atoms were calculated using the Hellman-Feynman theorem and the atoms relaxed until the forces had converged to less than 0.001 eV/Å and the pressure on the cell had equalized (constant volume). The GGA was applied using the parameterization of Perdew, Burke, and Ernzerhof[34] (PBE).

The crystal wave functions were expanded in terms of a plane wave basis set using periodic boundary conditions with the projector augmented wave method[35] employed to represent the core electrons (Bi: [Xe], O: [He]). The plane wave cutoff energy and *k*-point density, obtained using the Monkhorst-Pack[36] method, were both checked for convergence for each system to within 0.01 eV/Bi. A plane wave cutoff of 500 eV was implemented, with *k*-point grid densities of $4\times4\times4$ used for the α-phase, and a grid of $6\times6\times6$ *k*-points used for each of the three δ-Bi_2O_3 configurations.

B. Experiment

α-Bi_2O_3 was obtained commercially (Aldrich 99.99%), pressed into pellets at 5 tonnes and sintered at 700 °C. The phase integrity of the resulting ceramic pellets was confirmed by x-ray diffraction.

High-resolution x-ray photoemission spectra were measured in a Scienta ESCA 300 spectrometer. This incorporates a rotating anode Al $K\alpha$ ($h\nu$=1486.6 eV) x-ray source, a 7 crystal x-ray monochromator, and a 300 mm mean radius spherical sector electron energy analyzer with parallel electron detection system. The x-ray source ran with 200 mA emission current and 14 kV anode bias, with the analyzer operating at 150 eV pass energy with 0.8 mm slits. Gaussian convolution of the analyzer resolution with a linewidth of 260 meV for the x-ray source gives an effective instrument resolution of 350 meV. Samples were cleaned *in situ* by the rear face electron beam heating at 600 °C. The C 1*s* to O 1*s* XPS core level intensity ratio was reduced to below 0.01 by this cleaning procedure. Sample charging was problematic and it was necessary to stabilize the surface charge with an electron flood gun delivering 5 eV electrons. Binding energies were referenced to the very weak residual C 1*s* peak, which was assigned a binding energy of 285.0 eV.

X-ray absorption and emission spectra were measured at beamline 7.0.1 at the Advanced Light Source (ALS), Lawrence Berkeley National Laboratory. This beamline is equipped with a spherical grating monochromator.[37] Emission spectra were recorded using a Nordgren-type grazing-incidence spherical grating spectrometer.[38] For resonant emission experiments, the beamline was set to have an energy resolution of 350 meV at the O *K* edge, and the emission spectrometer was set to have a resolution of 360 meV. Absorption spectra were measured in total electron yield (TEY) mode by monitoring the sample drain current. The beamline resolution was set to 200 meV for these experiments. The absorption spectra were normalized to a reference current from a clean gold mesh positioned in the path of the photon beam.

III. α-Bi_2O_3

A. Computational results

Structural optimization calculations were performed at a series of volumes, allowing the atomic positions, the lattice vectors, and angles to relax within constrained total volume. The resulting energy volume curve was fitted to the Murnaghan equation of state[39] to obtain the equilibrium cell volume. The optimized structural parameters and the calculated binding energy are shown in Table I, with the predicted lattice vectors in good agreement with experimental values.[2] The calculated *a* and *b* lattice vectors are within 2% of experiment, with the *c* vector overestimated by just 1%. The calculated β angle of 112.82° compares well to the experimental value of 112.98°. Each Bi atom has a Bi nearest

TABLE I. Calculated binding energy and structural data for α-Bi_2O_3.

	α
ΔE (eV/Bi)	−14.53
Volume (Å^3)	346.38
a(Å)	5.959 (+1.9%)
b(Å)	8.318 (+1.9%)
c(Å)	7.580 (+1.0%)
β	112.82°

neighbor at 3.63 Å and five coordinated oxygen atoms at distances ranging from 2.19 Å to 2.59 Å (see Table II) giving rise to a highly asymmetric site.

The electron densities for the states between 0 eV and −12 eV (with respect to the highest occupied state) were calculated. Both O 2s and Bi 5d states lie outside this range. They have no significant role in bonding and have therefore been excluded from this analysis. A two-dimensional electron density slice has been made through the (100) plane containing Bi atoms for α-Bi_2O_3 and is shown in Fig. 3. An almost spherical electron distribution can be seen around the O atoms, while a strongly asymmetric density is clearly present around each Bi atom directed away from the oxygen nearest neighbors. This is indicative of a stereochemically active lone pair, The lone pairs occur in pairs directed towards each other and suggest the possibility of long-range Bi-Bi interactions.

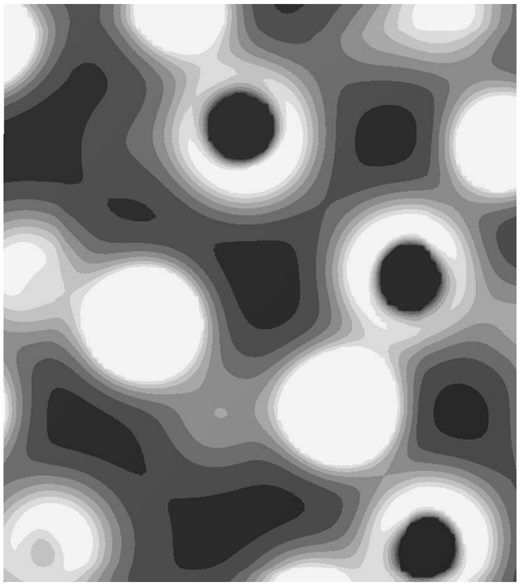

FIG. 3. Electron density contour maps of states from −12 eV to the highest occupied state of α-Bi_2O_3. Contour levels are shown between 0 (black) and 0.4 $e/Å^3$ (white).

The partial (l and m decomposed) electronic densities of states (PEDOS) are shown in Fig. 4 in the range from −12 eV to +6 eV (with respect to the highest occupied state). These were calculated by projecting the wave functions onto spherical harmonics centred on each atom with a radius of 1.65 Å for Bi and 1.55 Å for O. This ratio is consistent with the charge density maps and gives rise to the correct number of electrons and reasonable space filling. The qualitative results insensitive to a change in the radii.

The PEDOS contain a low energy peak (peak I), between −11 eV and −8 eV, which is mainly Bi 6s in nature with some O 2p character also present. This peak is positioned at significantly lower energies than the rest of the valence states. A group of peaks are present between −6 eV and the highest occupied state. This central block can be divided into three distinct regions. These run approximately from −6 eV to −3 eV (peak II), from −3 eV to −1.5 eV (peak III) and from −1.5 eV to the highest occupied state (peak IV). Peak II contains a mixture of O 2p and Bi 6p states while peak III consists mainly of O 2p states. The highest energy peak is dominated by O 2p states with some admixture of both Bi 6s and Bi 6p states. The presence of the Bi 6s character just below the Fermi level is somewhat unexpected as this energy is far above the main Bi 6s peak. α-Bi_2O_3 is calculated as having a band gap of 1.88 eV, in fair agreement with the experimental band gap of 2.5 eV.[40]

TABLE II. Nearest neighbor interatomic distances for α-Bi_2O_3.

Structure	A1-A2	d (Å)
α-Bi_2O_3	Bi-Bi	1×3.625
	Bi-O	1×2.587
		1×2.509
		2×2.283
		1×2.190

To examine the interactions in Bi_2O_3 and the states responsible for producing the lone pair on Bi we have calculated the partial electron density maps for the regions identified in the PEDOS. The states from −11 eV to −8 eV (peak I), display an enhanced density between Bi and O signifying a strong bonding interaction, Fig. 5(a). This bonding interaction between Bi 6s and O 2p orbitals explains the presence of O 2p states below the main O 2p block. The states from the centre of the valence band, between −6 eV

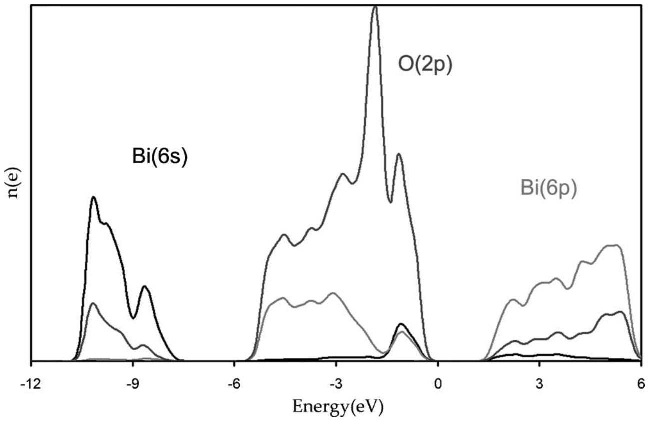

FIG. 4. Partial electron density of states of α-Bi_2O_3, plotted with respect to the highest occupied state. The black lines represent Bi 6s states, light grey Bi 6p states, and dark grey O 2p states.

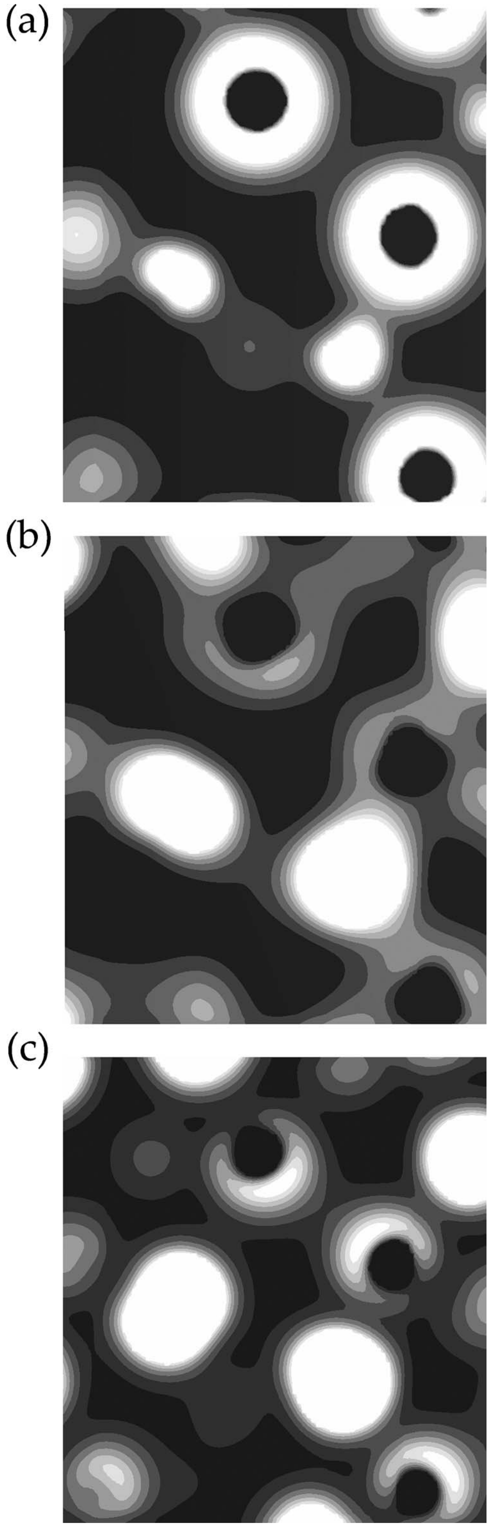

FIG. 5. Partial electron density contour maps for states from (a) −12 eV to −8 eV, (b) −6 eV to −1.5 eV, and (c) −1.5 eV to the highest occupied state for α-Bi_2O_3. Contour levels are shown between 0 (black) and 0.15 $e/Å^3$ (white).

TABLE III. Integrated COOP for the Bi 6*s*-O 2*p* and the Bi 6*p*-O 2*p* interactions occurring at the top and bottom of the valence band in α-Bi_2O_3.

	Region	α
Bi 6*s*-O 2*p*	−12 eV to −8 eV	1.06
Bi 6*s*-O 2*p*	−1.5 eV to 0 eV	−0.75
Bi 6*p*-O 2*p*	−1.5 eV to 0 eV	0.51

and −1.5 eV (peaks II and III), result in charge density which is centered mainly on the O atoms, with no contributions to the asymmetric electron density on Bi, Fig. 5(b). However, the electron density arising from the states at the top of the valence band between −1.5 eV to 0 eV (peak IV) shows a pronounced and asymmetric density on the Bi atoms. These states were found to be the sole source of asymmetry in the Bi electron distribution, Fig. 5(c). There is a noticeable lack of density present in the region between the Bi and O atoms suggesting an antibonding interaction. Filled antibonding states would explain the presence of Bi 6*s* character just below the Fermi level, at significantly higher energy than the main Bi 6*s* peak. The PEDOS show these states at the top of the valence band have a mixture of O 2*p*, Bi 6*s*, and Bi 6*p* character.

The underlying interactions can be identified using crystal orbital overlap populations[41] (COOP). Positive and negative COOP values correspond to bonding and antibonding interactions respectively. The integrated COOP for Bi 6*s*-O 2*p* and Bi 6*p*-O 2*p* interactions are listed in Table III. The large positive COOP (1.06) observed for the interaction between Bi 6*s* and O 2*p* in the region around −8 eV confirms that a strong bonding interaction occurs. This interaction of Bi 6*s* and O 2*p* also results in a filled antibonding combination between −1.5 eV and the Fermi level, as indicated by the large negative COOP (−0.75) observed for the interaction. This explains the presence of Bi 6*s* states at the top of the valence band in the PEDOS and the lack of density between the Bi and O atoms in the electron density maps for this region. The integrated COOP also confirm the presence of a bonding interaction between Bi 6*p* and the antibonding Bi 6*s*-O 2*p* states at −1 eV, as evident from the large positive value (0.51) observed for the interaction.

B. Experimental results

XPS of α-Bi_2O_3 in the region up to 35 eV binding energy is shown in Fig. 6. The spectrum is dominated by the shallow core Bi 5*d* spin orbit doublet with peaks at binding energies of 25.56 eV and 28.56 eV. The O 2*p* structure appearing at lower binding energy is a factor of 50 weaker than the shallow core level structure and appears to gain no intensity by mixing between O 2*p* and Bi 5*d* states. This contrasts strongly with HgO where the O 2*p* valence band intensity derives mainly from mixing with Hg 5*d* states.[24]

An expanded scan of the valence band XPS spectra of α-Bi_2O_3 is shown in the top left panel of Fig. 7 alongside the calculated electronic densities of states (EDOS) derived from the DFT calculations. The data for α-Bi_2O_3 are in general agreement with previously published data[42] but show better signal to noise and much better definition of the spectral features. It is convenient to discuss the structure of the valence band in terms of the same four features identified in the

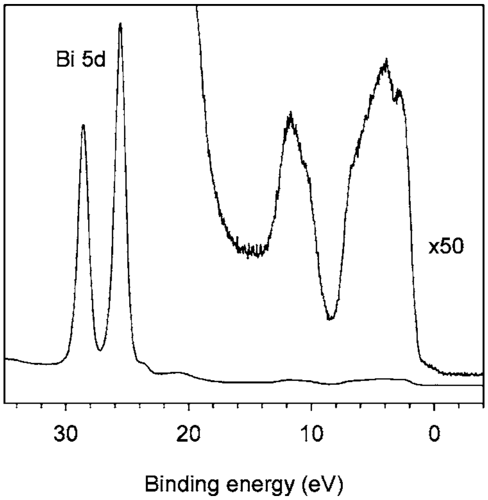

FIG. 6. XPS of α-Bi_2O_3 showing the shallow core Bi 5*d* levels and the valence band region.

DFT calculations, labelled I–IV. The lowest binding energy peak IV appears as a well-defined low binding energy shoulder on III, while II appears as a broader shoulder to high binding energy. Peak I, which appears at the highest binding energy of 12.4 eV, is well resolved from the rest of the valence band and shows signs of a low binding energy shoulder. The only discrepancy between the XPS and DFT results is that the overall energy spread of valence band states is less in the calculations than is found experimentally. This is a general problem when comparing EDOS derived from DFT calculations with experimental photoemission spectra.[43] For this oxide XPS appears to measure the total EDOS, suggesting that cross sections for ionization of O 2*p*, Bi 6*s*, and Bi 6*p* states are all very similar. This conclusion is in not in accord with the widely used ionization cross sections of Yeh and Lindau, where the Bi 6*p* and 6*s* one electron ionization cross sections are calculated to be much larger than the O 2*p* cross section.[44] This highlights the difficulty in using XPS data alone to try to derive information about the PEDOS.

The O *K* shell emission spectrum of α-Bi_2O_3 is shown in the lower left-hand panel of Fig. 7. It is possible to identify three main bands, corresponding to peaks I, II, and III in XPS. There are, however, very pronounced changes in relative intensities compared to the XPS data. Most strikingly the high binding energy band I is much weaker relative to II and III in XES as compared to XPS. Due to the localized nature of the O 1*s* core hole and the dipole selection rule operative in X-ray emission, the O *K* shell emission spectra involve decay from occupied states of O 2*p* character into an O 1*s* core hole. O *K* emission therefore directly measures the O 2*p* PEDOS. Thus the diminution in intensity of band I is a clear signature of the fact that the corresponding electronic states at the bottom of the valence band have less O 2*p* character than the states closer to E_F. This reduced contribution of the O 2*p* levels to the PEDOS in band I is also seen

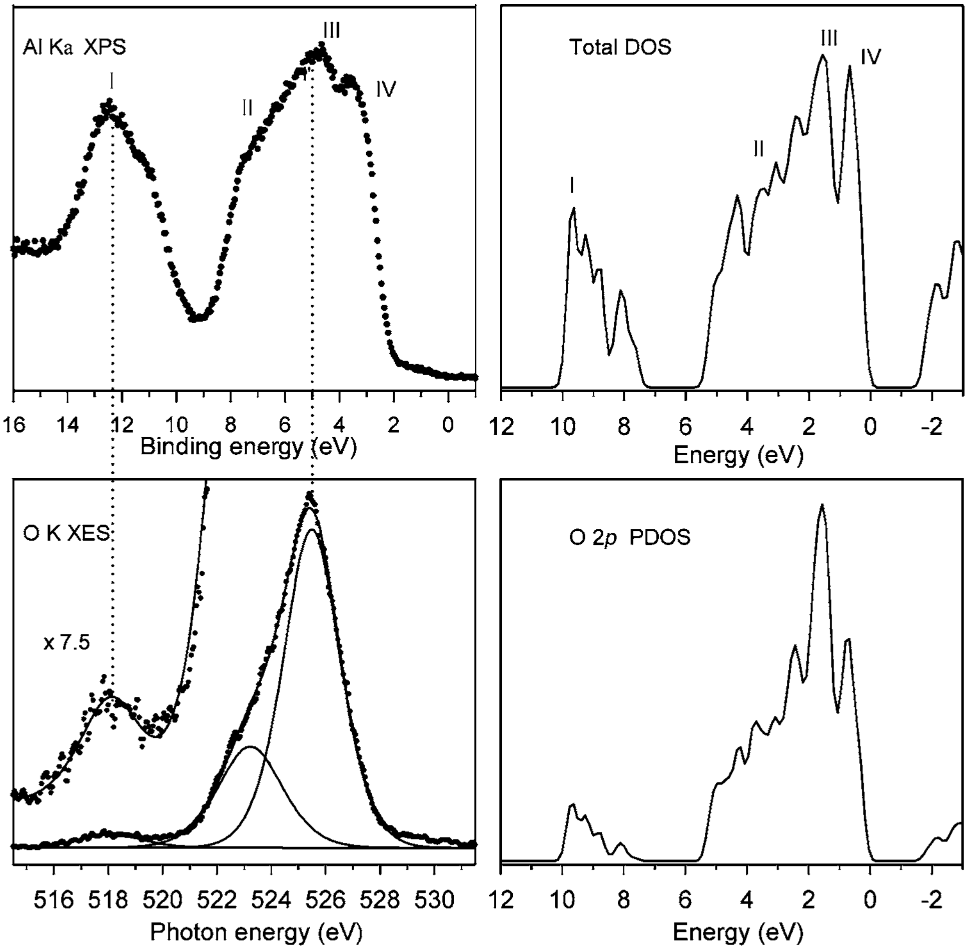

FIG. 7. Valence band Al $K\alpha$ XPS (upper left) and nonresonant O *K* shell XES (lower left) from α-Bi_2O_3 compared to the total DOS (upper right) and the O 2*p* PEDOS (lower right) derived from DFT band structure calculations. The alignment between the XPS and XES spectra is made on peak I. Note that the overall spread of energies is 17 eV in the experimental spectra but only 15 eV in the calculations.

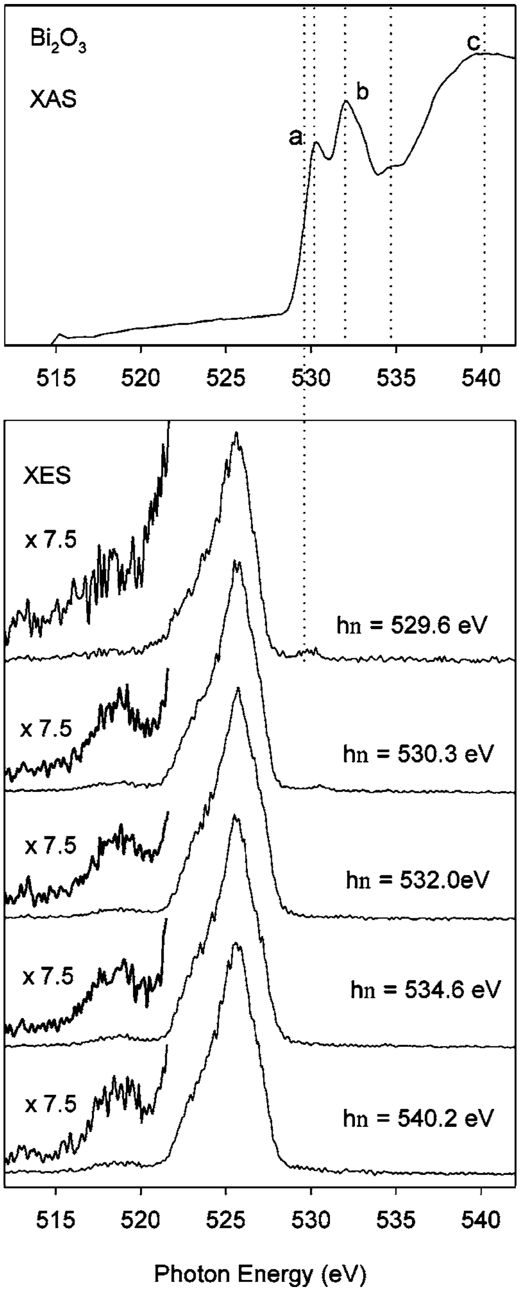

FIG. 8. Upper panel: O *K* shell x-ray absorption spectrum of α-Bi_2O_3. Lower panel: O *K* shell x-ray emission spectra of α-Bi_2O_3 excited at the photon energies indicated.

clearly in the calculations, where the states at the bottom of the valence band are mainly Bi 6*s* in nature.

The O *K* shell x-ray absorption spectrum of Bi_2O_3 is shown in Fig. 8, along with x-ray emission spectra excited at the energies indicated on the absorption spectrum. The absorption spectrum has two sharp peaks *a* and *b* above threshold, the second of which is stronger. A broader peak *c* is found at higher energy. Emission spectra were excited with photon energies between 529.6 eV and 540.2 eV, as indicated in the figure. The most striking change in the spectra is that the structure associated with Bi 6*s* states is very weak just above threshold and increases in intensity with increasing photon energy.

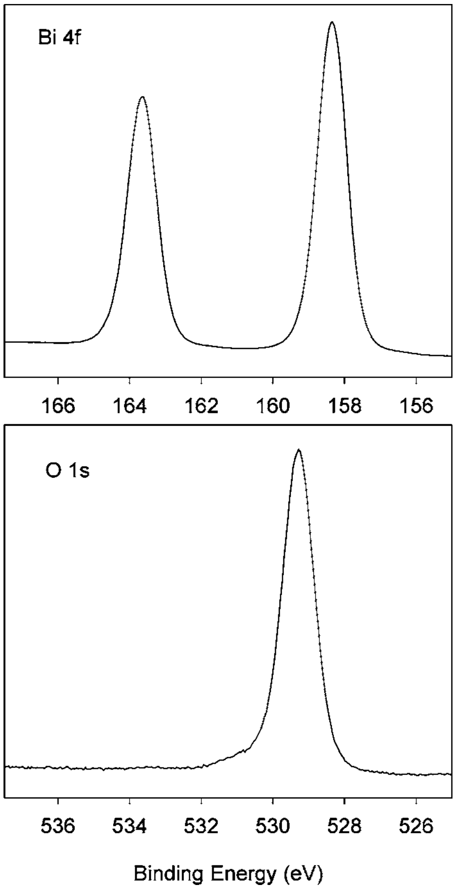

FIG. 9. The Bi 4*f* and O 1*s* core lines in Al $K\alpha$ XPS of α-Bi_2O_3.

The structure within the filled and empty densities of states may be used in turn to analyze the structure of loss structure due to high energy of the dominant core lines in XPS. The Bi 4*f* and O 1*s* core lines are shown in Fig. 9. The Bi 4*f* core lines may be fitted with a simple pair of Voigt functions with FWHM values of 0.95 eV and a spin-orbit splitting of 5.21 eV. The O 1*s* core line is dominated by a strong component at 529.28 eV with the FWHM of 1.03 eV and a much weaker component at 530.81 eV carrying about 5% of the spectral weight. The latter is probably associated with weak residual contamination. Scans over an extended energy range to high binding energy of these dominant core lines are shown in Fig. 10. To facilitate comparison of the Bi 4*f* and O 1*s* loss structure, the Bi $4f_{7/2}$ and O 1*s* lines have been aligned and the spectra are presented on an energy loss scale with these peaks set at zero. Loss structure is most clearly defined in the Bi 4*f* region where five distinct loss features A–E are observed. Some of the features (notably the sharp loss peak E) are mirrored with a second peak to 5.2 eV higher loss energy. This is an obvious consequence of the spin-orbit splitting of the Bi 4*f* core line. The strongest loss feature B is shifted by 16.2 eV from the core line and appears to correspond to the valence electron plasmon. The observed energy is significantly lower than the value of 18.3 eV that would be expected if both O 2*p* and Bi 6*s* electrons contributed to the electron density involved in the plasma oscillations, but is very close to the value of 16.6 eV

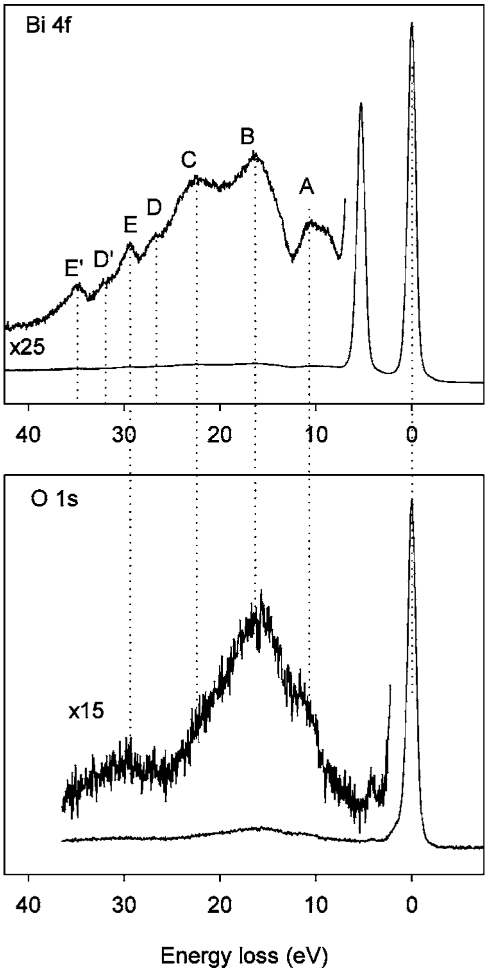

FIG. 10. The Bi $4f$ and O $1s$ core lines in Al $K\alpha$ XPS of α-Bi_2O_3 accumulated over an extended spectral range to show energy loss structure. The Bi $5f_{7/2}$ and O $1s$ core lines have been aligned in order to emphasize the relationship between the loss structures in the two spectra.

expected if only O $2p$ electrons are involved in the valence electron plasmon. The weaker peak A appears to correspond to the valence electron surface plasmon and appears at an energy roughly $1/\sqrt{2}$ that of A. The origin of peak C is unclear. Some of the intensity in this region must be associated with the $4f_{5/2}$ satellite of B, but the separation between the maxima of B and C (about 6.4 eV) is bigger than the spin-orbit splitting of the Bi $4f$ peaks. In addition peak C appears as a shoulder to B in the O $1s$ loss region. The prominent peak E appears 29.6 eV below the Bi $4f_{7/2}$ core line. This is very close to the separation between the Bi $5d_{5/2}$ shallow core level and the strong peak B above threshold observed in x-ray absorption spectra (Fig. 8). Thus the sharp peaks E and E' appear to correspond to excitation of the shallow core Bi $5d_{5/2}$ electrons into empty conduction band states. The weaker peaks D and D' correspond to excitation into the first peak above threshold A.

C. Discussion of α-Bi_2O_3

Examination of the calculated and experimental data shows the bonding in α-Bi_2O_3 to consist of interactions between Bi $6s$, Bi $6p$, and O $2p$. In particular, significant amounts of $6s$ states are found at the bottom of the valence band in both cases. The interaction of Bi $6s$ and O $2p$ results in filled bonding and antibonding combinations located in the regions around −9 eV and −1 eV, respectively. The strong coupling of unfilled Bi $6p$ with the antibonding states results in a net gain in energy, stabilizing the near Fermi level states and producing a strong asymmetric density projected out from the Bi atom (the Bi "lone pair"). This is a similar picture to that previously shown for lone pair formation in SnO (Refs. 24 and 25) and PbO (Refs. 26 and 27).

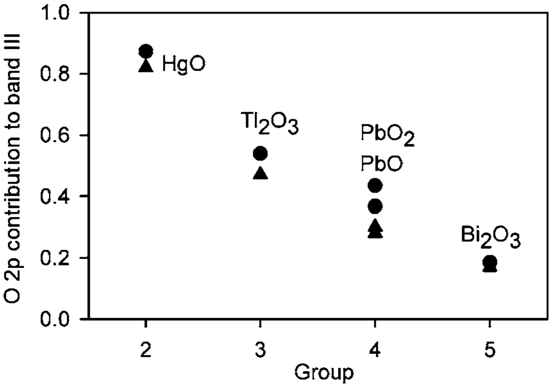

FIG. 11. Closed circles: estimated O $2p$ contribution to the lowest valence band state derived from intensities in O K shell XES spectra of the post-transition metal oxides HgO, Tl_2O_3, PbO_2, PbO, and Bi_2O_3 as a function of group number. Triangles: the ratio I(O $2p$)/[I(O $2p$)+I(Bi $6s$)] derived by integrating partial densities from DFT calculations across the lowest valence band state.

To quantify the idea of the contribution of O $2p$ levels to the PEDOS, it is possible to make an estimate of the O $2p$ contribution $f_{O\ 2p}$ to the lowest valence band state, where bonding between Bi $6s$ and O $2p$ is observed, as follows. The intensity I_l of the lowest valence band peak in XES is expressed as a fraction of the total valence band intensity I_{total} and this ratio is divided in turn by the number of metal atoms n per formula unit divided by the number of valence electrons pairs p per formula unit,

$$f_{O\ 2p} = \frac{(I_l/I_{\mathrm{total}})}{(n/p)}.$$

The results of this analysis for α-Bi_2O_3 are shown in Fig. 11, along with data for HgO, Tl_2O_3, PbO, and PbO_2 (Refs. 28, 29, and 45) and corresponding values obtained by integrating the PEDOS from the DFT calculations. Both the experimental and calculated data clearly show that there is a progressive decrease in the amount of O $2p$ character in the lowest valence band state (highest binding energy valence state) in moving across the Periodic Table. For α-Bi_2O_3 there is in fact only about 20% O $2p$ character present and we can therefore deduce that the states at the bottom of the valence band must have dominant cation $6s$ atomic character. We attempted to confirm this conclusion experimentally by observation of Bi N_3 emission spectra. Unfortunately the pronounced lifetime broadening of the N_3 level (5.7 eV in XPS) coupled with a low radiative yield precluded the possibility of obtaining useful data in this region. The shallower *O*3 level showed even more pronounced broadening with Lorentzian linewidth of 10.9 eV in XPS. In fact the experimental values displayed in Fig. 11 must represent the upper limits for the amount of O 2*p* character in the lowest valence band state, since the states in peaks I–IV are not of pure O 2*p* atomic character. The DFT calculations (Fig. 4) indicate there is a substantial cation 6*s* contribution to states at the top of band IV. There is also a significant 6*p* contribution to the states in band II. Experimental confirmation of the Bi 6*s* contribution to the top of the valence band (with a corresponding reduction in the amount of O 2*p* character) is provided by a careful comparison between the XPS and XES spectra. Thus for α-Bi_2O_3, the low binding energy peak band IV is much weaker in the XES spectrum than in the XPS spectrum, and no longer appears as a well-defined spectral feature. The O *K* shell x-ray absorption spectrum provides collaborating evidence that band I is associated with states of different atomic character to II and III, Fig. 11.

It has been shown that antibonding Bi 6*s* states are indeed present at the top of the valence band and that it is the coupling of cation *p* with the antibonding anion *s* and cation *p* states that is responsible for producing the directed asymmetric density on Bi. While the term "lone pair" is accurate in describing the resulting electron density around the atom it is misleading in that it overlooks the fact that the anion plays a key role in producing the states required to form this stereochemically active density. Our analysis predicts that changing the anion should have a strong effect on the resulting structure. Indeed experimentally Bi_2S_3 adopts an orthorhombic crystal structure, space group *Pbnm*, with kinked layers similar to those observed for SnS and SnSe, while Bi_2Se_3 and Bi_2Te_3 both adopt a more symmetric rhombohedral crystal structure.[1] This is in line with the anion having a strong effect on the resulting asymmetry in the electronic distribution of the cation.

IV. δ-Bi_2O_3

The high temperature δ phase of Bi_2O_3 adopts a defective fluorite structure with two oxygen vacancies per unit cell. The arrangement of oxygen vacancies and the oxygen conduction pathway are still matters of conjecture. The results for α-Bi_2O_3 indicate that oxygen plays a key role in the formation of lone pairs and hence the position of oxygen vacancies will effect the directionality of the lone pair through the symmetry of the remaining oxygen coordination. This is something which has not been considered previously but it will clearly have an impact on the stability of competing vacancy structures hence oxygen diffusion pathways.

Relaxation of cubic δ-Bi_2O_3 was carried out starting from an experimentally determined lattice constant of 5.665 Å.[18] The resulting structural optimization parameters of δ-Bi_2O_3 with oxygen vacancies aligned along the $\langle 100\rangle$, $\langle 110\rangle$, and $\langle 111\rangle$ directions are shown in Table IV. The calculated energies predict α-Bi_2O_3 to be more stable than δ-Bi_2O_3, as expected given that the former is the thermodynamically stable phase at low temperature. For δ-Bi_2O_3 the alignment of oxygen vacancies along $\langle 100\rangle$ is calculated to be the most favorable, with the $\langle 110\rangle$ and $\langle 111\rangle$ configurations of vacancies less stable by 0.06 eV/Bi and 0.54 eV/Bi, respectively. However, the $\langle 110\rangle$ vacancy configuration is in theory energetically accessible taking into account thermal energy in the order of 0.09 eV per particle above 730 °C, the temperature at which δ-Bi_2O_3 is formed. While previous LMTO-ASA (Ref. 14) and force field calculations[15,16] favored the $\langle 111\rangle$ alignment of vacancies, our results are in agreement with more recent GGA-DFT calculations.[17] Simple electrostatic arguments do favor the $\langle 111\rangle$ arrangement which allows the vacancies to be as far apart as possible. The fact we find the $\langle 100\rangle$ arrangement to be more stable indicates that more subtle effects are at play.

TABLE IV. Calculated energies (relative to α-Bi_2O_3) and structural data for the $\langle 100\rangle$, $\langle 110\rangle$, and $\langle 111\rangle$ oxygen vacancies configurations of δ-Bi_2O_3.

	$\langle 100\rangle$	$\langle 110\rangle$	$\langle 111\rangle$
ΔE (eV/Bi)	0.37	0.43	0.91
Volume (Å^3)	175.50	180.17	172.79
a(Å)	5.728	5.856	5.570
b(Å)	5.535	5.547	5.570
c(Å)	5.535	5.547	5.570
β	90°	90°	90°

For the $\langle 100\rangle$ and $\langle 110\rangle$ oxygen vacancy configurations relaxation of the lattice resulted in volume contractions of 3.5% and 1.0%, respectively, from the starting structure and a tetragonal distortion of the *a* vector, with $a:c$ ratios of 1.04 and 1.06. The oxygen vacancies are aligned along the *a* direction in the unit cell for both the $\langle 100\rangle$ and $\langle 110\rangle$ configurations. The relaxed $\langle 111\rangle$ configuration retains its cubic symmetry with a volume contraction of 5.0% from the starting structure. The observed volume contractions are not unexpected as this is a high temperature phase which we are modeling at 0 K. Each Bi has six nearest neighbor oxygen atoms ranging in distance from 2.31 Å to 2.55 Å. The closest Bi-Bi distance span a range from 3.87 Å for the $\langle 111\rangle$ configuration to 4.27 Å for the $\langle 110\rangle$ ordering of oxygen vacancies, Table V.

The calculated electron densities from the states between −12 eV and 0 eV (with respect to the highest occupied state) are shown for the three vacancy configurations in Fig. 12. For oxygen vacancies aligned along $\langle 100\rangle$, significant asymmetry is present on Bi, although it is substantially weaker than for α-Bi_2O_3, Fig. 12(a). This alignment creates a vacancy channel in the lattice, with the six O atoms coordinated on one side of the Bi atom and the asymmetric electron density directed into the vacancy channel. These lone pairs on Bi occur in pairs, directed towards each other. The electron density map for the $\langle 110\rangle$ alignment of vacancies shows similar asymmetry in the Bi electron density, Fig. 12(b). However, in this structure the Bi site is less distorted and no hollow channel is produced in the lattice. Four oxygen atoms are coordinated on one side of each Bi, with the asymmetric electron density directed towards the opposite side, where the two oxygen vacancies and two remaining coordinated oxygens are positioned. The Bi-O interatomic distance of

TABLE V. Nearest neighbor interatomic distances for the ⟨100⟩, ⟨110⟩, and ⟨111⟩ oxygen vacancies configurations of δ-Bi_2O_3.

Structure	A1-A2	d (Å)
⟨100⟩ δ-Bi_2O_3	Bi-Bi	2×4.189
	Bi-O	2×2.439
		2×2.399
		1×2.347
		1×2.305
⟨110⟩ δ-Bi_2O_3	Bi-Bi	2×4.273
	Bi-O	2×2.550
		4×2.347
⟨111⟩ δ-Bi_2O_3	Bi-Bi	4×3.872
	Bi-O	3×2.427
		3×2.371

these two oxygens is lengthened from 2.35 Å in the starting configuration to 2.55 Å in the optimized unit cell. It is only when the vacancies are aligned along ⟨111⟩ that no significant asymmetry in the electron density is observed, Fig. 12(c). Here a single oxygen vacancy is present on each side of the Bi atom, creating an almost symmetric Bi site. The electron density map shows centrosymmetric electron density around Bi, with no enhanced electron density directed towards the oxygen vacancy sites.

The calculated PEDOS for the three δ-Bi_2O_3 configurations are shown in Fig. 13. The PEDOS all share a number of common features with the α phase. The low energy peak, between −11 eV and −8 eV, and the three peaks in central blocks, −6 eV to −3 eV, −3 eV to −1.5 eV, and −1.5 eV to 0 eV are again all present. The main difference between the PEDOS of the α and δ phases arises from the states between −1.5 eV and 0 eV. In α-Bi_2O_3 the density of Bi 6p states present at the top the valence band almost equals that of the Bi 6s states. For the ⟨100⟩ alignment of vacancies in δ-Bi_2O_3 the contribution of Bi 6p states to the top of the valence band is significantly reduced. For the ⟨110⟩ alignment the contribution is even lower. The PEDOS from the ⟨111⟩ alignment of oxygen vacancies shows a flat contribution from the Bi 6p states at the top of the valence band different from that of the Bi 6s or O 2p states. The Bi 6p partial density of states does not drop to zero at the Fermi energy, thus producing metallic behavior. A similar feature was also observed for this alignment of vacancies in the studies performed by both Carlsson *et al.*[17] and Medvedeva *et al.*,[14] but was not examined and no explanation has been put forward for the apparent metallicity of this configuration.

To observe what impact the disparity in Bi 6p character has on the states at the top of the valence band we have calculated the charge density arising from states in the energy range −1.5 eV to 0 eV for each vacancy configuration, Fig. 14. For the ⟨100⟩ alignment of oxygen vacancies the electron density shows a directed asymmetric density on Bi similar to that observed for α-Bi_2O_3, Fig. 14(a). The ⟨110⟩ alignment results in somewhat weaker asymmetry in the Bi electron distribution, Fig. 14(b). Finally for the ⟨111⟩ alignment of vacancies there is only a weak elongation of the Bi electron density on each side of the Bi atoms, pointing towards the oxygen vacancies, Fig. 14(c).

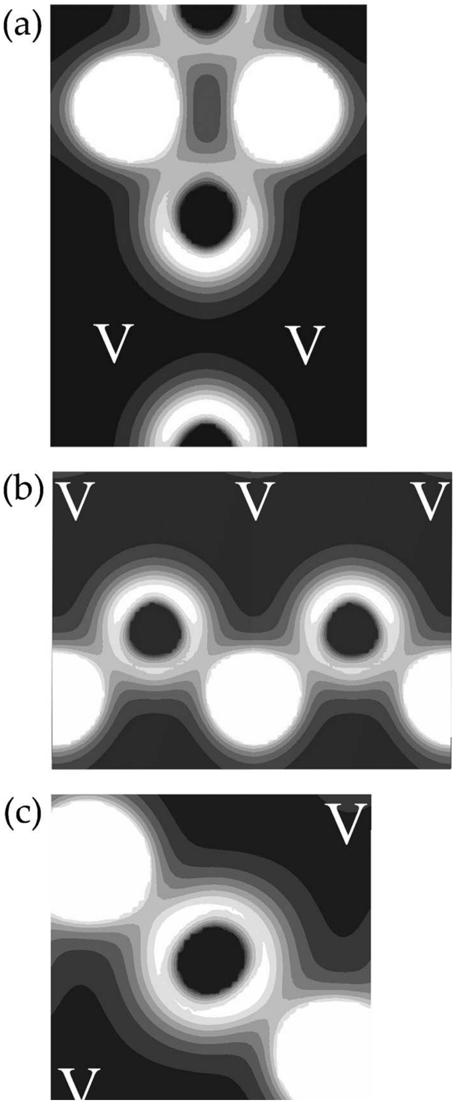

FIG. 12. Electron density contour maps of states from −12 eV to the highest occupied state for the (a) ⟨100⟩, (b) ⟨110⟩, and (c) ⟨111⟩ arrangement of oxygen vacancies in δ-Bi_2O_3, taken through the oxygen vacancy plane. Oxygen vacancy positions are marked by white V's. Contour levels are shown between 0 (black) and 0.4 $e/Å^3$ (white).

The integrated COOP confirm the presence of bonding and antibonding Bi 6s-O 2p interactions for each of the vacancy alignments in δ-Bi_2O_3, Table VI. The interaction between Bi 6p and the antibonding states is also present. It does however show greater variation, as may be expected from the differences in Bi 6p character present at the top of the valence band in each structure. For the ⟨100⟩ alignment of vacancies the coupling of Bi 6p with the antibonding states is reduced significantly from the COOP found for α -Bi_2O_3 (0.51) to 0.20. The reduced coupling is also indicated through the narrowing of the band gap, with unfilled Bi 6p dominating the lowest unoccupied states. The ⟨100⟩ alignment of vacancies creates the most distorted Bi site of the δ configurations which allows for relatively strong coupling of

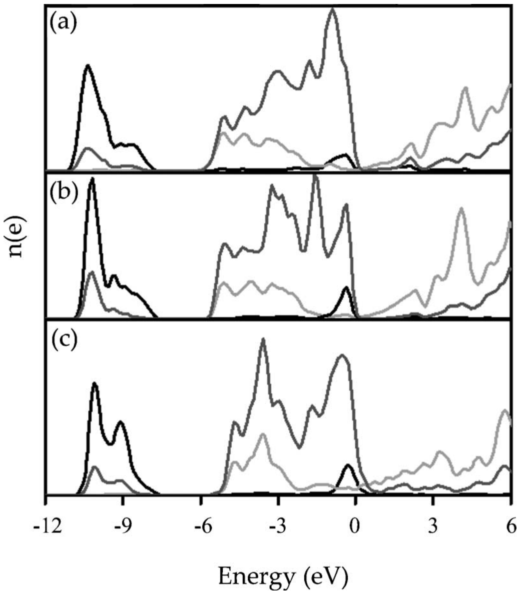

FIG. 13. Partial electron density of states of the (a) ⟨100⟩, (b) ⟨110⟩, and (c) ⟨111⟩ vacancy alignment configurations of δ-Bi_2O_3, plotted with respect to the highest occupied state. The black lines represent Bi 6*s* states, light grey represent Bi 6*p* states, and dark grey represent O 2*p* states.

Bi 6*p* and hence an active "lone pair" on Bi.

There is an absence of a "lone pair" for the ⟨111⟩ alignment of oxygen vacancies. As the Bi site is almost centrosymmetric, the coupling of Bi 6*p* states with the antibonding Bi 6*s* and O 2*p* states is severely restricted by parity considerations. The integrated COOP show a reduction in the interaction of Bi 6*p* levels with the antibonding states to just 0.08, the lowest value obtained for the three vacancy configurations. The Bi 6*p* states are clearly not interacting with the antibonding Bi 6*s* and O 2*p* states. However, this does not explain the significant amount of Bi 6*p* character present just below the Fermi level in the PEDOS. To investigate this further we have calculated the band structure for each vacancy alignment and show the results in Fig. 15.

While there is no indirect band gap present for any of the calculated vacancy configurations, a direct gap of 0.50 eV and 0.54 eV exists at the Γ point (0,0,0) for the ⟨100⟩ and ⟨110⟩ vacancy alignments, respectively. For the ⟨111⟩ alignment of vacancies the lowest lying conduction band is partially occupied at Γ. The bands between −10 eV and −8 eV are known from the projected EDOS and COOP to derive from a bonding interaction between O 2*p* and Bi 6*s* states. The splitting of bands in this region is caused by the gain in energy of those Bi 6*s* bands that undergo a bonding interaction with O 2*p*. For example at Γ (0,0,0) the site projections for the ⟨100⟩ alignments of vacancies show the upper combination at −8 eV is composed of 97% Bi 6*s* while the lower combination at −10 eV contains a mixture of 65% Bi(6*s*) and 35% O(2*p*). Large splitting of these bands occurs at Γ and $X\ (\frac{1}{2},0,0)$ for all vacancy alignments and also at Z $(\frac{1}{2},0,\frac{1}{2})$ for the ⟨100⟩ and ⟨111⟩ alignment of vacancies. This shows that the interaction between Bi 6*s* and O 2*p* is strongest at these points.

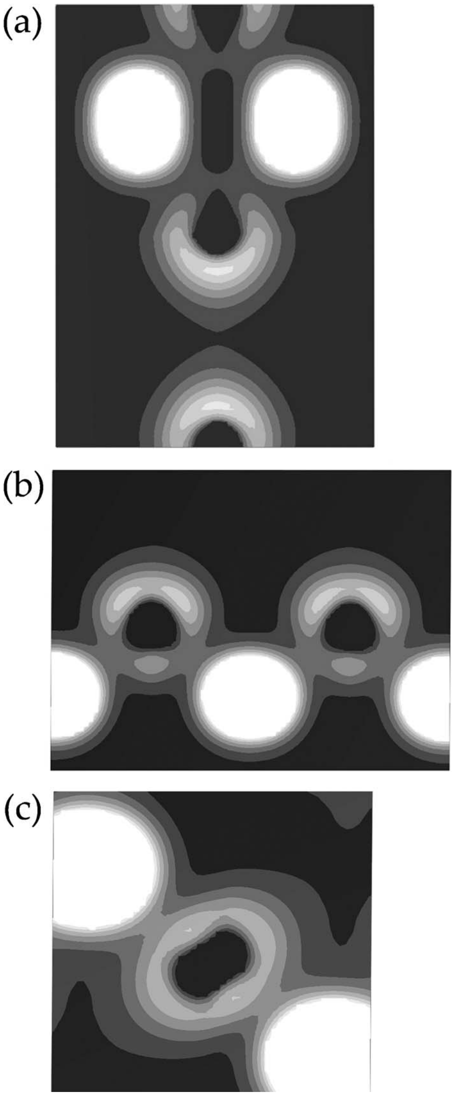

FIG. 14. Electron density contour maps of states from −1.5 eV to the highest occupied state for the (a) ⟨100⟩, (b) ⟨110⟩, and (c) ⟨111⟩ arrangement of oxygen vacancies in δ-Bi_2O_3, taken through the oxygen vacancy plane. Contour levels are shown between 0 (black) and 0.15 $e/Å^3$ (white).

Analysis of the partial electron density maps and COOP confirmed the states producing the Bi "lone pair" lie between −1.5 eV and 0 eV, resulting from the mixing of the antibonding Bi 6*s* and O 2*p* states with Bi 6*p*. The large number of bands in this region results in a complex band structure. For the ⟨100⟩ and ⟨110⟩ alignments of oxygen vacancies the lowest lying conduction band drops in energy to the Fermi level at Γ, while it is unoccupied elsewhere throughout the band structure. In these configurations the bands toward the top of the valence band are reduced in energy at Γ creating a direct band gap, suggesting that the strongest interaction of the Bi 6*s*-O 2*p* antibonding combination with Bi 6*p* occurs at Γ.

For the ⟨111⟩ alignment of vacancies the conduction band filled at Γ is shifted down in energy to approximately −2 eV. The site projections of this band at Γ consist of approximately 85% Bi 6*p* character with the remainder O 2*p*. The

TABLE VI. Integrated COOP for the Bi 6*s*-O 2*p* and the Bi 6*p*-O 2*p* interactions occurring at the top and bottom of the valence band in α-Bi_2O_3 and the ⟨100⟩, ⟨110⟩, and ⟨111⟩ oxygen vacancies configurations of δ-Bi_2O_3.

	Region	α	⟨100⟩	⟨110⟩	⟨111⟩
Bi 6*s*-O 2*p*	−12 eV to −8 eV	1.06	0.85	0.90	0.82
Bi 6*s*-O 2*p*	−1.5 eV to 0 eV	−0.75	−0.60	−0.65	−0.59
Bi 6*p*-O 2*p*	−1.5 eV to 0 eV	0.51	0.20	0.15	0.08

COOP showed that strong coupling between Bi 6*p* and O 2*p* states was absent in this region. therefore it is reasonable to assume that Bi 6*p*-Bi 6*p* interactions are the source of this strange behavior. To confirm this, the band decomposed charge density at Γ, from between −1.5 eV and 0 eV, is shown for the ⟨111⟩ configuration in Fig. 16. The electron density map for this section of the band structure shows strong delocalization of the electron density around the Bi

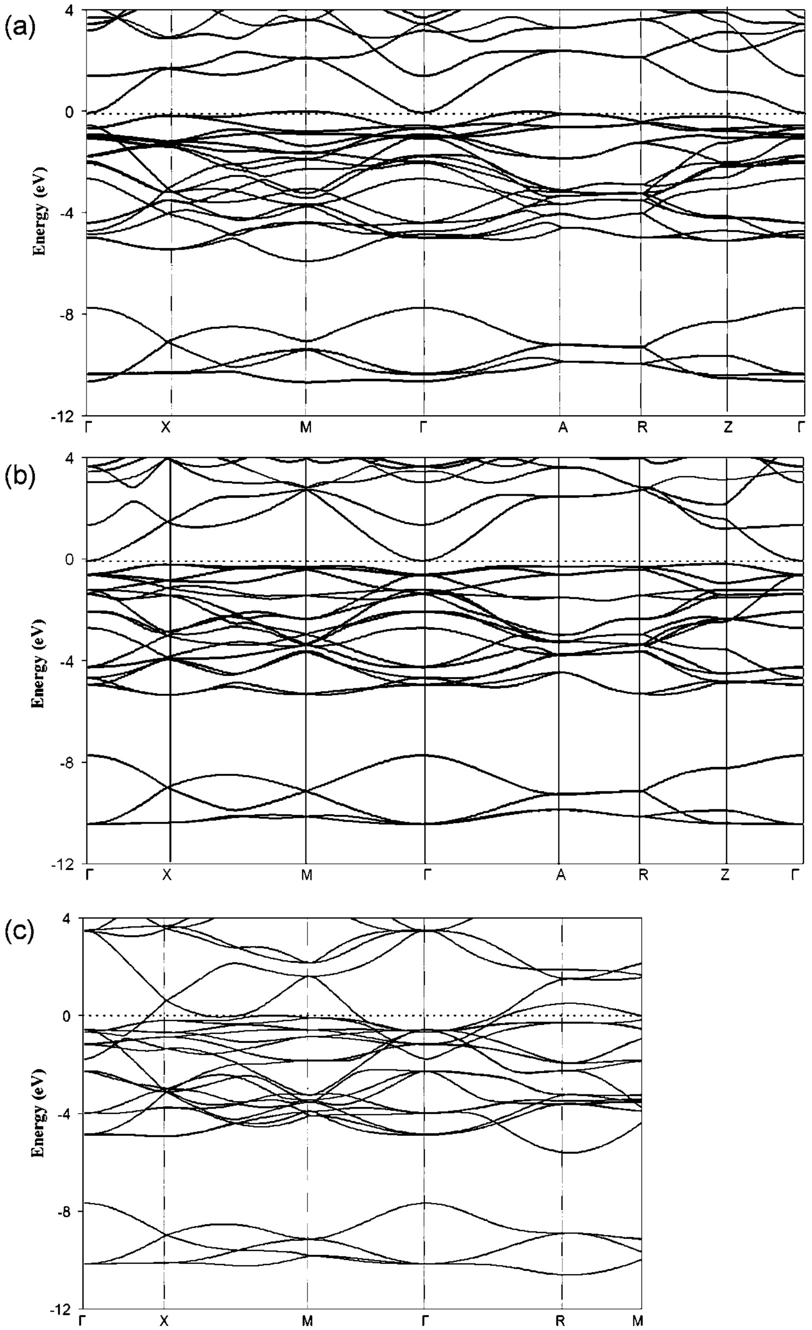

FIG. 15. The calculated band structure for the (a) ⟨100⟩, (b) ⟨110⟩, and (c) ⟨111⟩ alignments of oxygen vacancies in δ-Bi_2O_3, plotted with respect to the Fermi level.

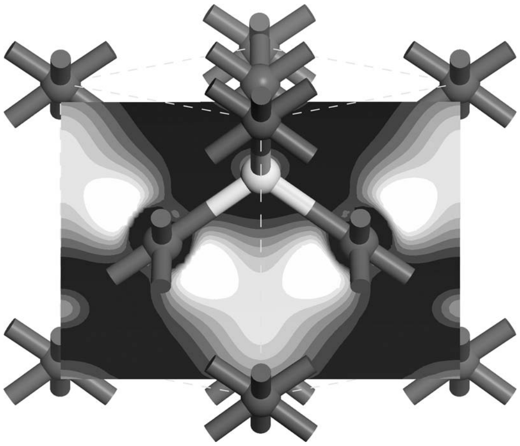

FIG. 16. Band decomposed electron density map, arising from states from between −1.5 eV to 0 eV at the Γ point of δ-Bi_2O_3 for oxygen vacancies aligned along ⟨111⟩. Contour levels are shown between 0 (black) and 0.1 $e/\AA^3$ (white).

atoms in the direction of the oxygen vacancies. There is a large overlap of density between neighboring Bi atoms indicating a strong interaction between the Bi 6*p* states. While the symmetric alignment of vacancies does not allow for formation of a "lone pair," it appears that at Γ this is in part compensated by these strong Bi-Bi interactions. This leads to the filling of previously unoccupied Bi 6*p* states and the shift of the lowest lying conduction band to more than −1.5 eV below the Fermi level.

These results give a good qualitative view of both bonding and lone pair formation in δ-Bi_2O_3 and indicate that the vacancy alignment has a strong impact on the both the energies and the electronic structure. The results show subtleties that a potential based approach would not identify or even consider, and suggest that careful thought should be given to the method used when modeling dynamics of structures containing ns^2 cations. Indeed this can also be extended to fast oxygen ion conductors in general. In a recent DFT study by Mohn *et al.*[46] of the distribution of oxygen vacancies in $Ba_2In_2O_5$, relatively few energetically stable configurations were found, at odds to classical approaches which predicted a random distribution of vacancies. These studies show that covalent metal-oxygen bonding is more important in determining the properties of these materials than previously thought and as such an electronic structure approach is required.

V. CONCLUSIONS

The electronic structure of α-Bi_2O_3 has been examined using a combination of theory and experiment. DFT was used to calculate the electronic density of states, electron density and the crystal orbital overlap populations. High resolution XPS, XES, and XAS were used to investigate both the core and valence band regions. Both approaches are in good agreement with respect to the electronic structure. Careful comparison of the XPS and XES spectra and DFT indicate that the majority of the Bi 6*s* states are present at low energy but with additional Bi 6*s* character at the top of the valence band. Detailed analysis indicates that it is the interaction of Bi 6*p* states with antibonding Bi 6*s* and O 2*p* states that is responsible for the asymmetric electron density on Bi. Our study shows that the electronic structure of α-Bi_2O_3, in particular the "lone pair" formed by Bi(III) is strongly influenced by the Bi-O bonding.

The calculations were extended to consider the ⟨100⟩, ⟨110⟩, and ⟨111⟩ oxygen vacancy configurations of δ-Bi_2O_3. The strongest asymmetry in the Bi electron distribution occurs for oxygen vacancies aligned along ⟨100⟩ which was also calculated to be the most energetically stable configuration. For the ⟨110⟩ configuration the interaction of Bi 6*p* is not as pronounced as for the ⟨100⟩ alignment although the structure is only 0.06 eV per Bi less stable. The ⟨111⟩ alignment of vacancies gives a centrosymmetric Bi site and is calculated as the most energetically unfavorable. This finding is at variance with previous force field calculations.[15,16] Our calculations show for the first time that the electronic structure of δ-Bi_2O_3, in particular the "lone pair" formed by Bi(III), has a strong dependence on the coordination of anions. The stability of different vacancy configurations indicates that the lone pair directly affects the vacancy location and hence the lone pair will be important in understanding oxygen diffusion in Bi_2O_3 and Bi containing oxygen ion conductors.

ACKNOWLEDGMENTS

We would like to acknowledge the HEA for a PRTLI (Cycle III) grant and TCD for a Trinity College Postgraduate Studentship. All calculations were performed on the ITTAC cluster as maintained by TCHPC. We are grateful to the UK EPSRC for support of the NCESS facility. The Boston University program is supported in part by the U.S. Department of Energy under Contract No. DE-FG02-98ER45680. The Advanced Light Source is supported by the Director, Office of Science, Office of Basic Energy Sciences, of the U.S. Department of Energy under Contract No. DE-AC02-05CH11231.

---

*Tel: +353 1 6081357; electronic address: watsong@tcd.ie

[1] R. W. G. Wyckoff, *Crystal Structures* (Kreiger, Melbourne, 1986), Vol. 2.
[2] H. A. Harwig, Z. Anorg. Allg. Chem. **444**, 151 (1978).
[3] L. G. Sillen, Ark. Kemi, Mineral. Geol. **12A**, 1 (1937).
[4] T. Takahashi and H. Iwahara, J. Appl. Electrochem. **3**, 65 (1972).
[5] E. C. Subbaro and H. S. Maiti, Solid State Ionics **11**, 317 (1984).
[6] P. Shuk, H. D. Wiemhöfer, U. Guth, W. Göpel, and M. Greenblatt, Solid State Ionics **89**, 179 (1996).
[7] A. Cabot, A. Marsal, J. Arbiol, and J. R. Morante, Sens. Actuators

B **99**, 1 (2004).

[8] T. Takeyama, N. Takahashi, T. Nakamura, and S. Ito, Opt. Mater. **26**, 413 (2004).

[9] E. D. Wachsman, J. Eur. Ceram. Soc. **24**, 1281 (2004).

[10] N. M. Sammes, G. A. Tompsett, H. Nafe, and F. Aldinger, J. Eur. Ceram. Soc. **19**, 1801 (1999).

[11] M. Yashima and D. Ishmura, Chem. Phys. Lett. **378**, 395 (2003).

[12] P. D. Battle, C. R. A. Catlow, J. W. Heap, and L. M. Moroney, J. Solid State Chem. **63**, 8 (1986).

[13] P. D. Battle, C. R. A. Catlow, J. Drennan, and A. D. Murray, J. Phys. C **16**, 561 (1983).

[14] N. I. Medvedeva, V. P. Zhukov, V. A. Gubanov, D. L. Novikov, and B. M. Klein, J. Phys. Chem. Solids **57**, 1243 (1996).

[15] P. W. M. Jacobs and D. A. Mac Donaill, Solid State Ionics **18**, 209 (1986).

[16] P. W. M. Jacobs and D. A. Mac Donaill, Solid State Ionics **23**, 279 (1987).

[17] J. M. Carlsson, B. Hellsing, H. S. Domingos, and P. D. Bristowe, Phys. Rev. B **65**, 205122 (2002).

[18] R. W. G. Wyckoff, *Crystal Structures* (Kreiger, Melbourne, 1986), Vol. 1.

[19] A. M. Azad, S. Larose, and S. A. Akbar, J. Mater. Sci. **29**, 4135 (1994).

[20] H. A. Harwig, Z. Anorg. Allg. Chem. **444**, 151 (1978).

[21] G. Gattow and H. Schröder, Z. Anorg. Allg. Chem. **318**, 176 (1962).

[22] A. Laarif and F. Theobald, Solid State Ionics **21**, 183 (1986).

[23] G. Mairesse, *Fast Ion Transport in Solids*, edited by B. Scrosati (Kluwer, Amsterdam, 1993), p. 271.

[24] G. W. Watson and S. C. Parker, J. Phys. Chem. B **103**, 1258 (1999).

[25] A. Walsh and G. W. Watson, J. Solid State Chem. **178**, 1422 (2005).

[26] A. Walsh and G. W. Watson, Phys. Rev. B **70**, 235114 (2004).

[27] A. Walsh and G. W. Watson, J. Phys. Chem. B **109**, 16686 (2005).

[28] P. A. Glans, T. Learmonth, K. E. Smith, J. Guo, A. Walsh, G. W. Watson, F. Terzi, and R. G. Egdell, Phys. Rev. B **71**, 235109 (2005).

[29] P. Glans, T. Learmonth, C. McGuiness, K. Smith, J. Guo, A. Walsh, G. W. Watson, and R. Egdell, Chem. Phys. Lett. **399**, 98 (2004).

[30] G. Kresse and J. Hafner, Phys. Rev. B **49**, 14251 (1994).

[31] G. Kresse and J. Furthmuller, Comput. Mater. Sci. **6**, 15 (1996).

[32] G. Kresse and J. Furthmuller, Phys. Rev. B **54**, 11169 (1996).

[33] W. Kohn and L. J. Sham, Phys. Rev. **140**, A1133 (1965).

[34] J. P. Perdew, K. Burke, and M. Ernzerhof, Phys. Rev. Lett. **77**, 3865 (1996).

[35] P. E. Blöchl, Phys. Rev. B **50**, 17953 (1994).

[36] H. J. Monkhorst and J. D. Pack, Phys. Rev. B **13**, 5188 (1976).

[37] J. Nordgren and R. Nyholm, Nucl. Instrum. Methods Phys. Res. A **246**, 242 (1986).

[38] J. Nordgren, G. Bray, S. Cramm, R. Nyholm, J. E. Rubensson, and N. Wassdahl, Rev. Sci. Instrum. **60**, 1690 (1989).

[39] F. D. Murnaghan, Proc. Natl. Acad. Sci. U.S.A. **30**, 244 (1944).

[40] T. P. Debbies and J. W. Rabalais, J. Chem. Phys. **20**, 277 (1977).

[41] R. Hoffmann, *Solids and Surfaces* (Wiley-VCH, New York, 1988), p. 42.

[42] T. P. Debies and J. W. Rabalais, Chem. Phys. **20**, 277 (1977).

[43] Y. Dou, R. G. Egdell, D. S. L. Law, N. M. Harrison, and B. G. Searle, J. Phys.: Condens. Matter **10**, 8447 (1998).

[44] J. J. Yeh and I. Lindau, At. Data Nucl. Data Tables **32**, 1 (1985).

[45] D. J. Payne, R. G. Egdell, A. Walsh, G. W. Watson, J. Guo, P.-A. Glans, T. Learmonth, and K. E. Smith, Phys. Rev. Lett. **96**, 157403 (2006).

[46] C. E. Mohn, N. L. Allen, C. L. Freeman, P. Ravindran, and S. Stølen, J. Solid State Chem. **178**, 346 (2005).